Model for partial coherence and wavefront curvature in grating interferometers

Ben McMorran and Alexander D. Cronin

Department of Physics, University of Arizona, Tucson, Arizona 85721, USA

We examine how partial coherence and wavefront curvature of beams affect interference fringes behind diffraction gratings. We simulate (1) the Talbot effect, (2) far-field diffraction, (3) Mach-Zehnader interferometers, (4) Talbot-Lau interferometers, and (5) Lau interferometers using a numerically efficient expression. We show how interference fringes in each case depend on the beam's initial width, its coherence width (transverse coherence length), and its wavefront curvature in directions both parallel and perpendicular to the grating bars. The separation between gratings and the rotational alignment of the gratings about the optical axis are also considered. The formula used for our simulations is derived using the mutual intensity function of a Gaussian Schell-model beam.

PACS number(s): 03.75.Dg, 42.25.Kb, 42.25.Hz

I. INTRODUCTION

Gratings illuminated by an optical beam imprint correlations in the beam's wave field, and these correlations lead to several distinct interference effects. For example, if an optical beam is sufficiently coherent, then downstream of a transmission grating one finds shadows of the grating bars, followed by Talbot revivals, and eventually far-field (Fraunhoffer) diffraction patterns. A second grating can be added to the setup to make doubly diffracted beams overlap, thus forming a Mach-Zehnder interferometer. However, if the optical beam is disordered, i.e., incoherent, then the Talbot revivals and far-field diffraction pattern get blurred, and the interferometer paths are harder to isolate. To analyze interference phenomena in general one needs a formalism that incorporates the beam's width, coherence width (transverse coherence length), and wavefront radius of curvature.

In this paper we derive an expression [Eq. (18)] that models (1) Talbot revivals, (2) far-field diffraction, (3) Mach-Zehnder interference fringes, (4) Talbot-Lau interference fringes, and (5) Lau interference fringes for realistic beams. The beam can be converging, collimated, or diverging and can have arbitrary coherence properties. Our single expression reproduces results found in the literature [1–5] on partially coherent beams, but our expression is unique in its versatility. Our model incorporates arbitrary beam properties (coherence widths, beamwidths, and wavefront curvatures) that are allowed to vary separately in two directions (perpendicular and parallel to the grating bars). Our model works for two arbitrarily located gratings, and allows for the second grating to be rotated about the optical axis (see Fig. 1). We assume monochromatic beams in this model, but the expression we derive can be integrated over wavelength to take longitudinal coherence into account. We developed this model to simulate an electron beam Lau interferometer that we built with nanostructure gratings [6]. But since this model applies to a broad range of interferometer designs, and lends itself to computationally efficient code, we present simulations for cases 1–5 above.

We include many coherence parameters efficiently by assuming a *Gaussian Schell-model* (GSM) beam. Just as Medina and Pozzi model electron holography and interferom-

etry experiments using partially coherent optical theory and GSM beams [7], we believe this analytical technique can appropriately model a wide variety of matter wave interferometer experiments [8]. The GSM beam is a statistical distribution of Gaussian beam modes [9] and is a particular example of a field emitted from a Collett-Wolf source [10,11]. While Gaussian beams became popular in the early 1960s with the advent of laser physics, the GSM source was first described in the late 1970s as a tool to simulate partially coherent beams while still using some mathematical properties of Gaussian modes.

This paper is divided into two sections. In the first section, we derive our model by calculating the *mutual intensity function* of a GSM beam throughout the optical setup in Fig. 1. The mutual intensity function is a tool to keep track of the intensity, coherence width, and phase of a partially coherent optical field. It is similar to many mathematical quantities such as the cross correlation function, the cross spectral density function, and the mutual coherence function, which are all defined in [12] and [13]. We use the standard definition for mutual intensity,

$$J(\boldsymbol{\rho}_a, \boldsymbol{\rho}_b; z) = \langle \psi^*(\boldsymbol{\rho}_b, z, t) \psi(\boldsymbol{\rho}_a, z, t) \rangle_t, \quad (1)$$

where here ψ represents the wave-field amplitude for a Gaussian mode and the angular brackets refer to averaging
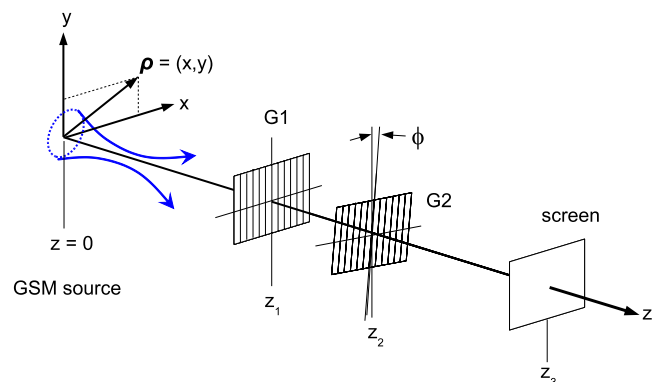

FIG. 1. (Color online) Optical setup. A GSM beam starts at $z = 0$. Transmission grating G1 is located at z_1. The second grating G2 is located at z_2. A screen for viewing intensity patterns is located at z_3.

013601-1

over a statistical distribution (described in Sec. II A) of such modes [14]. The coordinate z is along the GSM beam axis, and $\boldsymbol{\rho}_a$ and $\boldsymbol{\rho}_b$ are two transverse coordinates in a plane of constant z (see Fig. 1). $J(\boldsymbol{\rho}_a, \boldsymbol{\rho}_b)$ describes both the intensity profile of the beam and the degree of spatial coherence of the waves in the beam. The intensity can be calculated by evaluating the mutual intensity function with $\boldsymbol{\rho}_a = \boldsymbol{\rho}_b$, i.e.,

$$I(\boldsymbol{\rho};z) = J(\boldsymbol{\rho}, \boldsymbol{\rho};z). \tag{2}$$

In the second half of the paper, we use this model to simulate the optical intensity distribution throughout a variety of interferometers under different illumination conditions. Partially coherent illumination blurs the distinction between these different types of interferometers, so we offer a classification scheme to distinguish them based on the coherence widths of the beam at various locations. We discuss how the transition from Talbot revivals to far-field diffraction behind a single grating depends on the incident beam properties, and how transverse coherence affects Mach-Zehnder, Talbot-Lau, and Lau interference fringes.

II. PROPAGATION OF A GSM BEAM THROUGH A TWO-GRATING SYSTEM

We first explain how the mutual intensity of a GSM beam $J^{(0)}$ evolves through space by computing the propagation of an initial wave field from an initial plane to a plane just before the first grating. Then we calculate the mutual intensity for a beam that has passed through a single grating. Finally we derive the mutual intensity function describing the optical field beyond two gratings.

A. GSM beam in free space

We begin by supposing that a semicoherent optical beam has a known mutual intensity function $J^{(0)}$ in the plane $z=0$. We take a Gaussian Schell-model beam [13,15] whose mutual intensity between two points $\boldsymbol{\rho}_a$ and $\boldsymbol{\rho}_b$ is

$$J^{(0)}(\boldsymbol{\rho}_a, \boldsymbol{\rho}_b;0) = e^{-\pi[(\boldsymbol{\rho}_a + \boldsymbol{\rho}_b)^2/4w_0^2 + (\boldsymbol{\rho}_a - \boldsymbol{\rho}_b)^2/\ell_0^2 + i(\boldsymbol{\rho}_a^2 - \boldsymbol{\rho}_b^2)/\lambda r_0]}, \tag{3}$$

where λ is the wavelength, w_0 is the beamwidth, ℓ_0 is the "coherence width" or "transverse coherence length," and r_0 is the radius of curvature for the wave front. As we discuss in [8], here we use the coherence width rather than the commonly used correlation width [16], since the coherence width cannot be wider than the beam. Equation (3) describes a distribution of quasimonochromatic Gaussian beams. Each Gaussian beam in the ensemble has an identical waist and similar radius of curvature, but there is a distribution of these Gaussian beams with principal axes tilted with respect to the GSM beam axis and a fluctuating relative phase. De Santis *et al.* showed that one way to make a GSM beam is to locate an extended source behind two consecutive, Gaussian-weighted, apertures and a lens [17]. If we generalize De Santis *et al.*'s result to allow the lens an arbitrary focal length, we believe this adequately represents the converging and partially coherent electron de Broglie wave source that we use for interfer-

ometry [6] and diffraction [18] experiments. Indeed, we are not the first to model an electron beam with a partially coherent GSM beam—Medina and Pozzi do so in [7]. Additionally, in [8] we show how a GSM beam can approximate the partially coherent slit-collimated beams commonly used in matter wave interferometry experiments.

To simplify forthcoming derivations, we express Eq. (3) in terms of an average coordinate and a separation vector, such that $\boldsymbol{\rho} \equiv (\boldsymbol{\rho}_a + \boldsymbol{\rho}_b)/2$ and $\Delta\boldsymbol{\rho} \equiv \boldsymbol{\rho}_a - \boldsymbol{\rho}_b$:

$$J^{(0)}(\boldsymbol{\rho}, \Delta\boldsymbol{\rho};0) = e^{-\pi(\boldsymbol{\rho}^2/w_0^2 + \Delta\boldsymbol{\rho}^2/\ell_0^2 + i2\boldsymbol{\rho}\cdot\Delta\boldsymbol{\rho}/\lambda r_0)}. \tag{4}$$

To determine the mutual intensity at some other location, we make use of the paraxial approximation to Zernike's general propagation law for fields with arbitrary coherence properties (see the Appendix). We that find $J^{(0)}(z)$ for isotropic beams is

$$J^{(0)}(\boldsymbol{\rho}, \Delta\boldsymbol{\rho};z) = \frac{w_0^2}{w(z)^2} e^{-\pi[\boldsymbol{\rho}^2/w(z)^2 + \Delta\boldsymbol{\rho}^2/\ell(z)^2 + i2\boldsymbol{\rho}\cdot\Delta\boldsymbol{\rho}/\lambda r(z)]}. \tag{5}$$

Equation (5) is written in terms of the *new* beamwidth, coherence width, and radius of wave-front curvature at a distance z from the origin. These are related to the initial beam properties (at $z=0$) as follows:

$$w(z) = w_0 \sqrt{\left(1 + \frac{z}{r_0}\right)^2 + \left(\frac{\lambda z}{w_0 \ell_0}\right)^2}, \tag{6}$$

$$\ell(z) = \ell_0 \sqrt{\left(1 + \frac{z}{r_0}\right)^2 + \left(\frac{\lambda z}{w_0 \ell_0}\right)^2}, \tag{7}$$

$$r(z) = z\left(\frac{(1 + z/r_0)^2 + (\lambda z/w_0\ell_0)^2}{(z/r_0)(1 + z/r_0) + (\lambda z/w_0\ell_0)^2}\right). \tag{8}$$

Equation (6) can be used to calculate the divergence or convergence angle θ_w of the GSM beam far away from the GSM beam waist, also known as the "angular spread of the beam" [13]:

$$\tan \theta_w = \frac{\lambda}{\ell_{\min}}, \tag{9}$$

where $\ell_{\min}$ is the coherence width at the GSM beam waist. The coherence width also diverges, but at a smaller angle $\theta_\ell \approx \lambda/w_{\min}$ called the "far-zone coherence angle" [13]. It is interesting to note that neither the GSM beamwidth nor the GSM beam coherence width evolves exactly like the diameter of a pure Gaussian beam. However, the ratio of coherence width to beamwidth in Eqs. (6) and (7) remains unchanged as the beam propagates through free space. That is,

$$\beta \equiv \frac{\ell(z)}{w(z)} = \text{const.} \tag{10}$$

β is known as the "degree of global coherence" [12,13]. If β is equal to unity, Eqs. (6)–(8) describe the beam diameter and radius of wave-front curvature for a standard (fully coherent) Gaussian beam.

Beams used in real experiments often have properties that differ between the horizontal ($\hat{x}$) and vertical ($\hat{y}$) directions. Therefore we consider an *anisotropic* two-dimensional GSM

beam that has different properties in the horizontal and vertical transverse directions:

$$J^{(0)}(\boldsymbol{\rho}, \Delta\boldsymbol{\rho}; z) = J^{(0)}(x, \Delta x; z) J^{(0)}(y, \Delta y; z)$$

$$= \frac{w_{x0}}{w_x(z)} e^{-\pi[x^2/w_x(z)^2 + \Delta x^2/\ell_x(z)^2 + i2x\Delta x/\lambda r_x(z)]}$$

$$\times \frac{w_{y0}}{w_y(z)} e^{-\pi[y^2/w_y(z)^2 + \Delta y^2/\ell_y(z)^2 + i2y\Delta y/\lambda r_y(z)]}.$$

$$(11)$$

Such an anisotropic GSM beam was first described by Li and Wolf [19]. The intensity of the beam in the region before the first grating G1 is given by

$$I^{(0)}(\boldsymbol{\rho}; z) = J^{(0)}(\boldsymbol{\rho}, \Delta\boldsymbol{\rho} = 0; z) = \frac{w_{x0}}{w_x(z)} \frac{w_{y0}}{w_y(z)} e^{-\pi[x^2/w_x(z)^2 + y^2/w_y(z)^2]}.$$

$$(12)$$

B. GSM after transmission through one grating

We now model how a single grating modifies the incident GSM beam [Eq. (11)]. The grating is a periodic structure, and so its complex transmission function can be described by a Fourier series:

$$t(\boldsymbol{\rho}) = t(x) = \sum_{m=-\infty}^{\infty} a_m e^{-i2\pi mx/d_1}, \quad (13)$$

where a_m is the mth (possibly complex) Fourier component describing the grating with period d_1, and we have assumed for this case that the grating is thin and that its inverse lattice vector is in the $\hat{x}$ direction. The mutual intensity function directly after the first grating is

$$J^{(1)}(\boldsymbol{\rho}, \Delta\boldsymbol{\rho}; z_1) = t^*\left(x - \frac{\Delta x}{2}\right) t\left(x + \frac{\Delta x}{2}\right) J^{(0)}(\boldsymbol{\rho}, \Delta\boldsymbol{\rho}; z_1)$$

$$= \sum_{m,m'=-\infty}^{\infty} a_{m'}^* a_m e^{-(i2\pi/d_1)(x\Delta m + \Delta x\bar{m})} J^{(0)}(\boldsymbol{\rho}, \Delta\boldsymbol{\rho}; z_1),$$

$$(14)$$

where $\bar{m} \equiv (m+m')/2$ and $\Delta m \equiv m - m'$. Equation (14) has two sums because the transmission function appears twice in the mutual intensity [once for $\psi^*(\boldsymbol{\rho}_b)$ and once for $\psi(\boldsymbol{\rho}_a)$ in Eq. (1)].

We again use Zernike's technique to propagate the mutual intensity distribution beyond the grating (see the Appendix). The actual form of the mutual intensity is complicated and does not lend much insight. Instead we present the intensity profile of a GSM beam after it has propagated an arbitrary distance z_{12} beyond a single grating, obtained from the mutual intensity by setting $\Delta\boldsymbol{\rho} = 0$:

$$I^{(1)}(\boldsymbol{\rho}; z_2) = J^{(1)}(\boldsymbol{\rho}, \Delta\boldsymbol{\rho} = 0; z_2)$$

$$= \frac{w_{x0}}{w_x(z_2)} \frac{w_{y0}}{w_y(z_2)} e^{-\pi y^2/w_y(z_2)^2} \sum_{m,m'=-\infty}^{\infty} a_{m'}^* a_m$$

$$\times e^{-\pi(x - \bar{m}\lambda z_{12}/d_1)^2/w_x(z_2)^2}$$

$$\times e^{-(i2\pi\Delta m/d_1)(x - \bar{m}\lambda z_{12}/d_1)(1 - z_{12}/r_x(z_2))}$$

$$\times e^{-\pi(\Delta m\lambda z_{12}/\ell(z_2)d_1)^2}. \quad (15)$$

C. GSM after transmission through two gratings

We now model a second grating (G2 in Fig. 1) located at z_2 that has a grating period d_2 and is rotated about the optical axis by an angle ϕ. Its complex transmission function is

$$t_2(\boldsymbol{\rho}) = \sum_{n=-\infty}^{\infty} b_n e^{-i2\pi n(x\cos\phi + y\sin\phi)/d_2}, \quad (16)$$

where b_n is the nth Fourier component describing the second grating.

Similarly to Eq. (14), the field directly behind the second grating is described by

$$J^{(2)}(\boldsymbol{\rho}, \Delta\boldsymbol{\rho}; z_2) = t_2\left(\boldsymbol{\rho} + \frac{\Delta\boldsymbol{\rho}}{2}\right) t_2^*\left(\boldsymbol{\rho} - \frac{\Delta\boldsymbol{\rho}}{2}\right) J^{(1)}(\boldsymbol{\rho}, \Delta\boldsymbol{\rho}; z_2).$$

$$(17)$$

This field then propagates beyond G2 to the plane z_3. The calculation of the mutual intensity function in this region is tedious but straightforward, so we opt here to present only the intensity profile. Thus, the intensity distribution of a GSM beam after two gratings is

$$I^{(2)}(\boldsymbol{\rho}, z_3) = \frac{w_{x0}}{w_x(z_3)} \frac{w_{y0}}{w_y(z_3)} \sum_{m,m',n,n'=-\infty}^{\infty} a_{m'}^* a_m b_{n'}^* b_n$$

$$\times D_{\bar{n}}^{\bar{m}}(\boldsymbol{\rho}, z_3, w_{x,y}(z_3)) F_{\Delta n}^{\Delta m}(\boldsymbol{\rho}, z_3, r_{x,y}(z_3))$$

$$\times P_{\bar{n}, \Delta n}^{\bar{m}, \Delta m}(z_3, r_{x,y}(z_3)) V_{\Delta n}^{\Delta m}(z_3, \ell_{x,y}(z_3)), \quad (18a)$$

where the beamwidth $w(z)$, coherence width $\ell(z)$, and radius of wave-front curvature $r(z)$, which can all differ between the horizontal and vertical directions, are given by Eqs. (6)–(8). There is a quadruple sum over Fourier components a_m and b_n, which describe gratings G1 and G2, respectively. Expressing indices of the sum as averages and differences, such that $\bar{m} \equiv (m+m')/2$ and $\Delta m \equiv m - m'$ and likewise for n, simplifies the notation. For conceptual purposes, here we have chosen to express each term in the sum as the product of four functions (D, F, P, and V), each of which describes a particular aspect of the diffraction pattern behind the two gratings. Each of these functions is dependent on the position of the two gratings (z_1 and z_2), their period (d_1 and d_2), and their relative rotation angle (ϕ). The overall shape of the diffraction pattern is described by

$$D_{\bar{n}}^{\bar{m}}(\boldsymbol{\rho}, z_3, w_{x,y}(z_3))$$

$$= \exp\left\{\frac{-\pi\left[x - \lambda z_{23}\left(\dfrac{\bar{n}\cos\phi}{d_2} + \dfrac{\bar{m}}{d_1}\dfrac{z_{13}}{z_{23}}\right)\right]^2}{w_x(z_3)^2}\right\}$$

$$\times \exp\left[\frac{-\pi\left(y - \dfrac{\bar{n}\sin\phi\lambda z_{23}}{d_2}\right)^2}{w_y(z_3)^2}\right]. \quad (18b)$$

Interference fringes within this diffraction envelope are described by

$$
\begin{aligned}
&F_{\Delta n}^{\Delta m}(\boldsymbol{\rho}, z_3, r_{x,y}(z_3)) \\
&= \exp\left\{ -i2\pi x \left[\frac{\Delta n \cos \phi}{d_2}\left(1 - \frac{z_{23}}{r_x(z_3)}\right) \right.\right. \\
&\quad \left.\left. + \frac{\Delta m}{d_1}\left(1 - \frac{z_{13}}{r_x(z_3)}\right) \right]\right\} \\
&\quad \times \exp\left[-i2\pi y \frac{\Delta n \sin \phi}{d_2}\left(1 - \frac{z_{23}}{r_y(z_3)}\right) \right]. \quad (18c)
\end{aligned}
$$

A phase factor, which describes the lateral shift and periodic contrast of fringes along the optical axis, is denoted by

$$
\begin{aligned}
&P_{\bar{n},\Delta n}^{\bar{m},\Delta m}(z_3, r_{x,y}(z_3)) \\
&= \exp\left[\frac{i2\pi\lambda z_{13}\Delta m}{d_1}\left(\frac{\bar{n}\cos\phi}{d_2} + \frac{\bar{m}}{d_1}\right)\left(1 - \frac{z_{13}}{r_x(z_3)}\right) \right] \\
&\quad \times \exp\left\{ \frac{i2\pi\lambda z_{23}\Delta n}{d_2}\left[\frac{\bar{m}\cos\phi}{d_1}\left(1 - \frac{z_{13}}{r_x(z_3)}\right) \right.\right. \\
&\quad \left.\left. - \frac{\bar{n}z_{23}}{d_2}\left(\frac{\cos^2\phi}{r_x(z_3)} + \frac{\sin^2\phi}{r_y(z_3)}\right) \right]\right\}. \quad (18d)
\end{aligned}
$$

The visibility of interference fringes as a function relative to grating position and orientation is described by

$$
\begin{aligned}
&V_{\Delta n}^{\Delta m}(z_3, \ell_{x,y}(z_3)) = \exp\left\{ \frac{ -\pi\left[\lambda z_{23}\left(\dfrac{\Delta n \cos \phi}{d_2} + \dfrac{\Delta m}{d_1}\dfrac{z_{13}}{z_{23}}\right) \right]^2 }{\ell_x(z_3)^2} \right\} \\
&\quad \times \exp\left[-\pi\left(\frac{\Delta n \sin \phi \lambda z_{23}}{d_2 \ell_y(z_3)}\right)^2 \right]. \quad (18e)
\end{aligned}
$$

Equation (18) is the main result of this paper. To summarize, it is a general expression for the intensity distribution of a partially coherent Gaussian Schell-model beam anywhere beyond two gratings ($z_3 > z_2$ in Fig. 1). It is valid for beams with two different coherence widths, two beamwidths, and two radii of wave-front curvature (one for each transverse direction) in the paraxial (Fresnel) approximation.

D. Fringe visibility as a function of grating rotation

Equation (18) describes how interference fringes become less visible when there is a relative rotation (ϕ) between gratings. By looking at just the first few Fourier components of the series contributing to interference fringes ($\Delta m, \Delta n = 0, \pm 1$), one can see that the fringe contrast is proportional to the last two terms in Eq. (18). In particular, note that for small angles ($\sin \phi \approx \phi$ and $\cos \phi \approx 1$) the very last term in the expression is responsible for the dependence of fringe visibility V on grating alignment:

$$
V \propto \exp\left[-\pi\left(\frac{\lambda z_{23}\phi}{d_2 \ell_y(z_3)}\right)^2 \right]. \quad (19)
$$

From this it is evident that fringe contrast decreases when the gratings are rotated with respect to one another, as expected.

As one application for this theory, in an upcoming study we show how one can use this rotational dependence of fringe visibility to measure coherence width in a beam, even if that length is far less than a grating period.

III. SIMULATION OF GRATING INTERFEROMETERS

Several types of interferometers have been constructed using gratings: Talbot, Mach-Zehnder, Talbot-Lau, and Lau. These interferometers are associated with different requirements for beam coherence. For instance, Talbot and Mach-Zehnder interferometers are often described in terms of fully coherent beams ($\beta = 1$), whereas Talbot-Lau and Lau interferometers can operate with incoherent beams ($\beta = 0$). However, real beams are *partially* coherent (with $0 < \beta < 1$), and we can use Eq. (18) to simulate how the degree of coherence β affects the salient features of any interferometer. Furthermore, beams can be diverging or converging. Equation (18) describes these cases too, with explicit allowance for the radius of curvature in the $\hat{x}$ and $\hat{y}$ directions. Since Eq. (18) works for a wide range of conditions, we use it explore interferometer configurations in between the simplest cases. The most useful result of this model, we believe, is its ability to assess the sensitivity of various interferometers to phase objects by showing how beam components propagate. We also note that with partial coherence and finite wave-front curvature a general way to classify these interferometers is by the coherence width of the beam at various locations (Table I).

In the following sections we describe each of these four interferometers in more detail, and illustrate how Eq. (18) can simulate them all with a wide variety of beams. For all simulations, we model $\lambda = 500$ nm light incident on identical binary transmission gratings with period $d_1 = d_2 = d = 10$ μm. We emphasize that Eq. (18) is well suited for rapid computation; each simulation in this paper takes under 20 s to evaluate on a PC. In a particular plane z_3, the intensity at each point can be evaluated with a quadruple sum that contains $\sim 10^4$ terms (m, m', n, n' each ranging from -4 to 4), the vast majority of which can be discarded beforehand by calculating the weighting factors $a_{m'}^* a_m b_{n'}^* b_n V_{\Delta n}^{\Delta m}(z_3, \ell_{x,y}(z_3))$. These considerations provide orders of magnitude computational savings over a Huygens wavelet approach, which would typically require a sum over 10^8 source points (10^2 points for each grating window $\times 10^2$ windows, in each of the $\hat{x}$ and $\hat{y}$ directions) to model a partially coherent source and skewed gratings.

A. Single-grating diffraction simulations (Talbot interferometer)

The optical field immediately behind a transmission grating has shadows of the grating bars. The shadows are followed by near-field (Fresnel) diffraction effects including Talbot revivals if $\ell(z_1) > d$. Next comes a gray zone where the Talbot revivals have reduced visibility if $\beta < 1$. Finally, far-field (Fraunhoffer) diffraction patterns emerge if $\ell(z_1) > d$. Figure 2 plots $I^{(1)}(x, y = 0; z_2)$ by evaluating Eq. (15). The three rows of Fig. 2 show the effect of different coher-

TABLE I. Conditions for various grating interferometers. Gratings may be placed in the near field (NF) or far field (FF) of each other. Interference fringes may be too closely spaced to resolve with an imaging detector, so a third grating (G3) can be used as a mask to observe them. Interferometers with significantly diverging or converging beams will require gratings with different periods (especially the Lau diffractometer).

Talbot	Mach-Zehnder	Talbot-Lau	Lau
Coherent beam needed	Coherent beam needed	Incoherent beam OK	Incoherent beam OK
	G2 in FF of G1	G2 in NF of G1	G2 in NF of G1
G2 in NF of G1	G3 in FF of G2	G3 in NF of G2	G3 in FF of G2
$\ell(z_1)>d_1$	$\ell(z_1)>d_1$	$\ell(z_1)<d_1$	$\ell(z_1)<d_1$
$\ell(z_2)>z_{12}\lambda/d_1$	$\ell(z_2)<z_{12}\lambda/d_1$	$\ell(z_2)<z_{12}\lambda/d_1$	$\ell(z_2)<z_{12}\lambda/d_1$
		$\ell(z_3)<z_{12}\lambda/d_1$	$\ell(z_3)>z_{12}\lambda/d_1$

ence widths, and the right-hand column shows the effect of a converging beam (a negative radius of curvature) at the plane $z=0$.

Since their discovery in 1836, the Talbot revivals have been described in over 300 articles, many of which are cited in Patorski's review of the field [20]. The phenomenon is known as the Talbot effect, and the intensity pattern shown in Fig. 2 is often referred to as the Talbot carpet. The revivals that are in phase (spatially registered) with the grating are separated by the Talbot distance $z_T=2d_1^2/\lambda$ if the incident beam has infinite radius of curvature. Equally prominent self-images occur at half the Talbot distance, but these are displaced transverse to the beam by half the grating period. The "higher-order Talbot effect" refers to the fringes with a period finer than the grating period. All of these effects are efficiently simulated with Eq. (15).

A second grating (G2) can be used as a mask to selectively transmit or block the beam flux and thus study the Talbot revivals without imaging the fringes directly. This is known as a Talbot interferometer. An imaging detector behind G2 (with spatial resolution potentially much coarser than d) allows one to study phase objects or abberations in the beam that displace some of the Talbot revivals [21]. Talbot revivals are visible in the region behind G1 where the separation between diffraction orders does not yet exceed the coherence width. This determines the maximum separation between the two gratings in a Talbot interferometer: $z_{12} < \ell(z_2)\lambda/d$.

When the radius of curvature is finite, as in a converging beam incident on the grating, then the Talbot carpet changes accordingly (see Fig. 2, right column). Reference [22] used this effect to measure the focal length of a lens. Diffraction orders can be resolved in the focal plane (Fig. 2, right center), as we demonstrated with converging electron beam diffraction from a nanograting [18]. Batelaan and co-workers observed electron diffraction from a nanograting with a more coherent and collimated beam (e.g., Fig. 2, left top) in Ref. [23].

Beyond the focused beam waists the orders can overlap again, and interfere (see Fig. 2, right top). This "one-lens one-grating" interferometer makes visible interference fringes if the coherent convergence angle ($\approx l_0/r_0$) is larger than the diffraction angle (λ/d). Hence, for converging beams the sequence of phenomena can be shadows, the Tal-

bot carpet, far-field diffraction, and then near-field diffraction again due to the diffracted beams overlapping once more.

B. Mach-Zehnder interferometer simulations

A Mach-Zehnder interferometer, like a Talbot interferometer, requires $\ell(z_1)>d$. However, the second grating G2 is located in the far field of G1, where there is no coherent overlap between diffraction orders [i.e., where $\ell(z_2) < z_{12}\lambda/d_1$]. Interference fringes occur where doubly diffracted beams overlap again as shown in Fig. 3. To read out the fringes, a third grating (G3) located at $z=z_3$ can serve as a mask to transmit intensity to a large-area (integrating) detector; this is how Pritchard and co-workers built an atom interferometer using thin nanostructure gratings [24].

Fringes remain visible along the optical axis until the doubly diffracted beams are displaced further than the coherence width, i.e., visibility requires that $\lambda(z_{12}-z_{23})/d<\ell(z_3)$, as described by Eq. (18e). Thus, if the coherence width decreases, the fringes get more localized along the optical axis. Measurements of contrast as a function of the grating separation difference ($z_{12}-z_{23}$) in a Mach-Zehnder interferometer [25,26] thus serve to measure the coherence width of an atom beam. Even incoherent beams still make intensity modulations due to a "position echo" [27] at exactly $z_{12} = z_{23}$.

The fringe period may also change as a function of z_3 due to wave-front curvature. Hence, measurements using G3 as a mask can report a fringe contrast that oscillates and even has zeros as G3 is moved to different planes z_3 [28]. However, this is an artifact of G3 having a different period than the fringes.

If the diffracted beams can be resolved at the second grating, such that $w(z_2)<z_{12}\lambda/d_1$, one obtains a separated path Mach-Zehnder interferometer. This provides an opportunity to insert a phase-shifting element in one beam of the diamond-shaped interferometer, and leave the reference beam unaffected. The resultant phase shift of the interference fringes has been used in numerous interferometric measurements (see Refs. [29,30] for examples in atom interferometry). We use Eq. (18) to show how a focusing lens can improve the path separation in Mach-Zehnder interferometers. Beams that are about as wide as the maximum path separation (Fig. 3, center column) are undesirable to the ex-
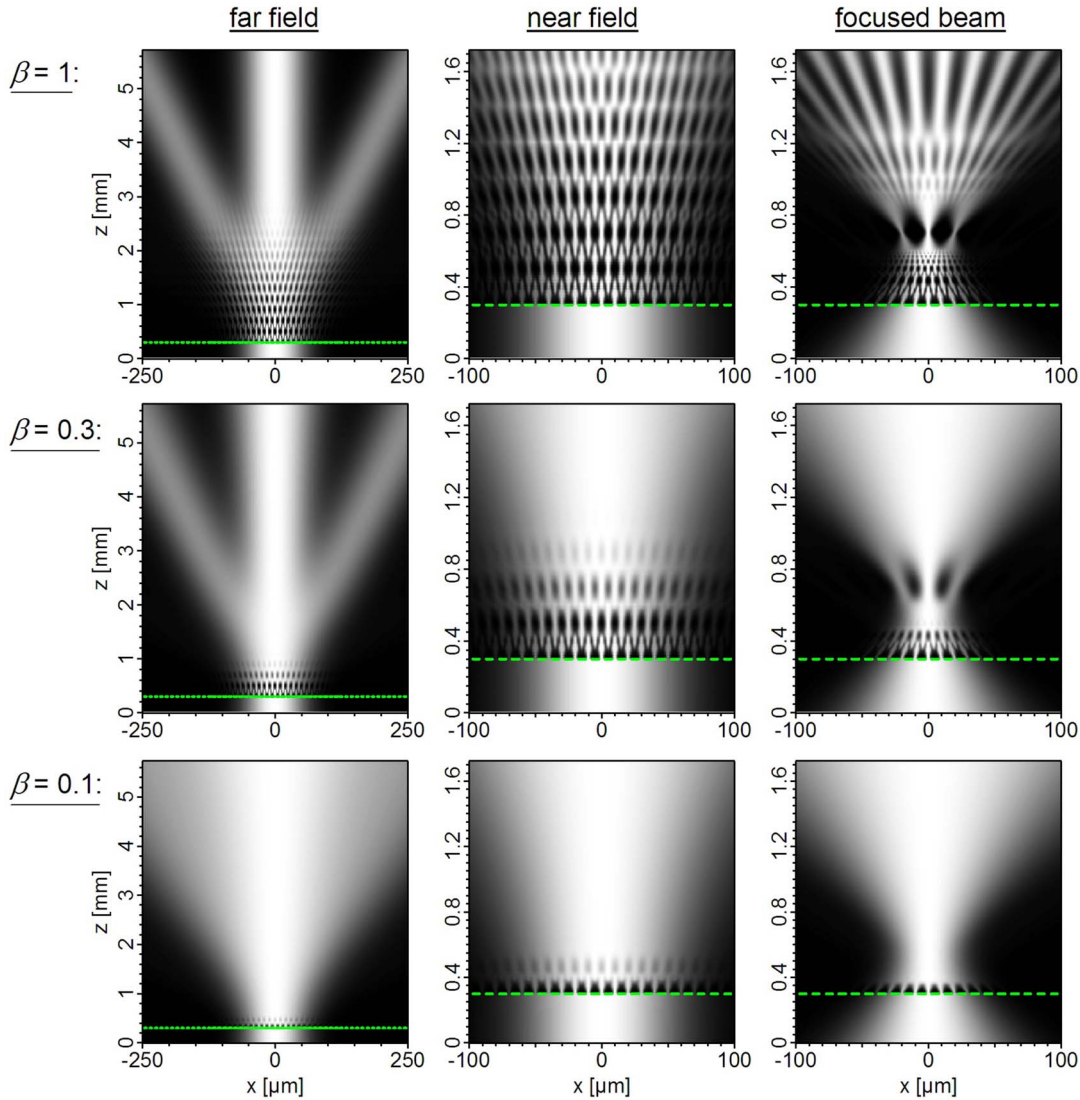
FIG. 2. (Color online) Simulations of diffraction of beams with wavelength $\lambda = 500$ nm from a single grating located at $z_1 = 0.3$ mm, modeled using Eq. (15). The left column features a GSM beam with $w_0 = 100$ μm and $r_0 = \infty$, the center column shows the same beam in a smaller field of view, and the right column shows a focused beam with $w_0 = 100$ μm and $r_0 = -0.7$ mm. The top row displays fully coherent beams ($\ell_0 = w_0$), the middle row simulates beams with $\ell_0 = 30$ μm, and the bottom row shows beams with $\ell_0 = 10$ μm. For presentation purposes, the simulations of intensity have been normalized so that each plane z has the same maximum intensity. Without this artificial rescaling, the intensity would be much higher near the beam waist and would drop by 60% after the grating (which here has 4-μm-wide slits with period $d_1 = 10$ μm).

perimentalist who wants to influence only one path. However, a lens can be used to separate the paths in a Mach-Zehnder interferometer, even for quite incoherent beams ($\beta = 0.1$ in the lower right image).

C. Talbot-Lau interferometer simulations

Interferometers can also be made with incoherent beams, for which the coherence width is less than a grating period [$\ell(z_1) < d$]. In this case the Talbot carpet is washed out, so the two-grating Talbot interferometer (with an integrating detector) yields no contrast. However, fringes are formed in several planes behind G2 (Fig. 4). One way to understand this is to imagine that each slit in G1 acts like a point source that causes a coherent diffraction pattern behind G2. While each slit source in G1 emits independently from all the other sources, the diffraction pattern intensities behind G2 can all line up when the two gratings are spaced by just the right distance. A Talbot-Lau interferometer normally uses a third grating (G3) as a mask to study the fringes in the near field of G2. Typically, the three gratings are separated by exactly half the Talbot length ($z_{12} = z_{23} = d^2/\lambda$), but other configurations are possible [31].

As shown in Fig. 5, the fringe visibility depends on wavelength, which verifies that the Talbot-Lau design is a wave-optics interferometer. A classical moiré (ray optics) model predicts the intensity variations precisely at $z_{23} = z_{12}$ [32], but only wave optics correctly predicts the visibility of these modulations and their oscillation with λ.
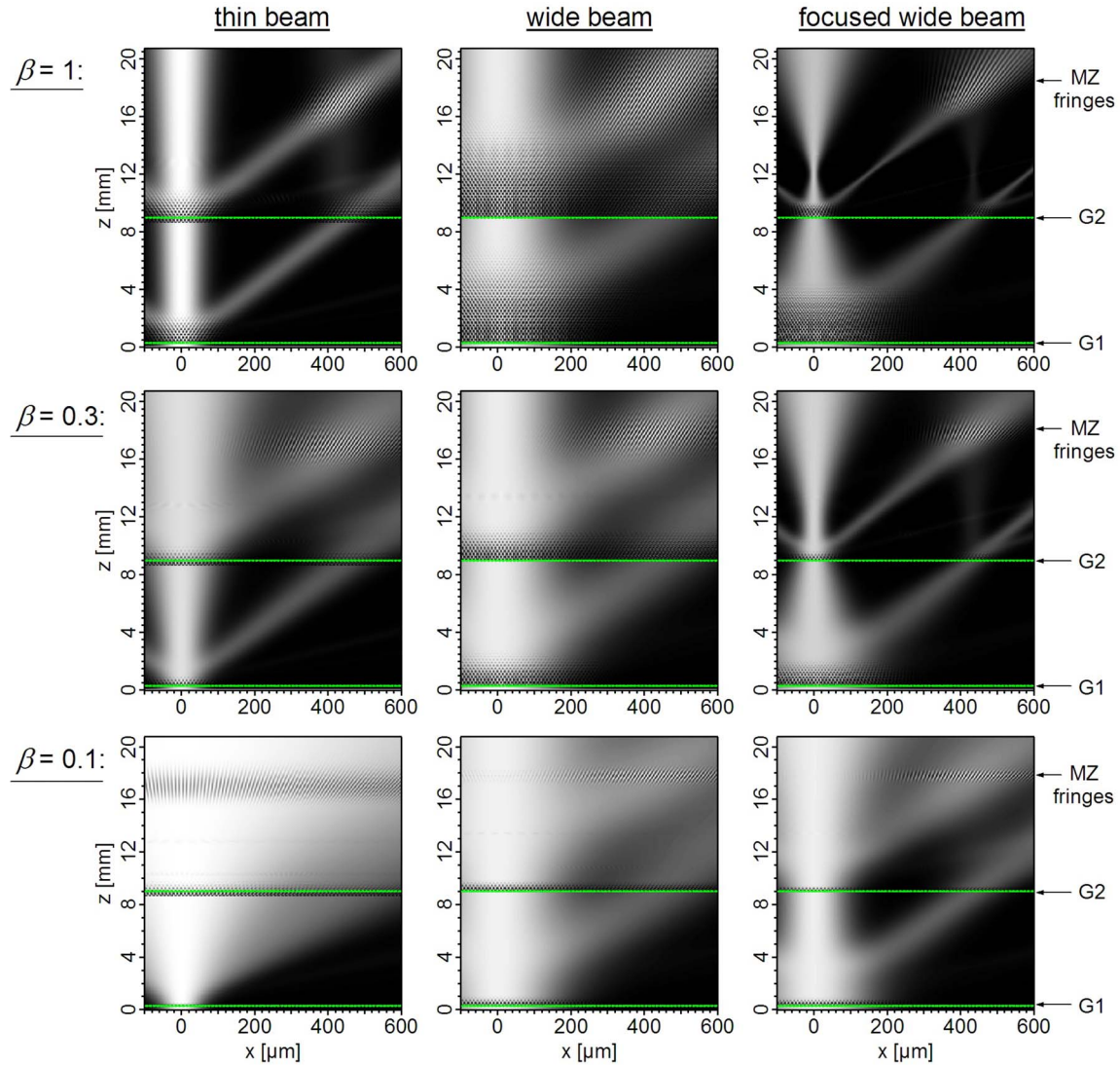
FIG. 3. (Color online) Mach-Zehnder interferometer simulations. The left column shows a thin beam that has initial width w_0 $=100$ μm, the middle column features a wide beam with $w_0=300$ μm, and the right column uses a wide but focused beam described by $w_0=300$ μm and $r_0=-12$ mm. The top row displays fully coherent beams ($\ell_0=w_0$), the middle row simulates beams with $\ell_0=30$ μm, and the bottom row shows beams with $\ell_0=10$ μm. Mach-Zehnder fringes are localized around $x=435$ μm and $z=17.7$ mm. The $\lambda=500$ nm beam is incident on binary transmission gratings G1 and G2 located at $z_1=0.3$ mm and $z_2=9$ mm, respectively. The gratings both have period $d=10$ μm and 50% open fraction and they are rotationally aligned. For presentation purposes, each row (corresponding to position z) of the intensity in these figures has been normalized to 1.

The Talbot-Lau interferometer is known for the fact that arbitrarily wide and incoherent beams can be used. However, the range in z_3 where contrast is high becomes more restricted for wider and less coherent beams (Fig. 4, bottom right). Still, a much smaller source brightness is required to observe interference fringes with this design as compared to a Mach-Zehnder interferometer. Furthermore, because the gratings and detector are located in the near-field, the Talbot-Lau is an easier interferometer to build for beams with short wavelengths (e.g., large-molecule interferometers [33]).

D. Lau interferometer simulations

In a Lau interferometer interference fringes can be formed far behind two gratings even when the gratings are illumi-nated by completely incoherent light [20,34,35]. In the far field of G2, after the Talbot-Lau fringes fade away, a set of courser fringes emerge. This happens where the expanding beams develop a sufficient coherence width to satisfy $\ell_x(z_3) > \lambda z_{12}/d$. If the beam is completely incoherent at the first grating, this is the location beyond which the fringe period exceeds the beam diameter at the first grating $w(z_1)$. Hence, Lau interferometers work with arbitrarily incoherent beams but they require beams with a finite width $w(z_1)$ and a detector in the far field.

The visibility of Lau fringes depends on grating separa-tion z_{12} as shown in Figs. 6 and 7. In particular, Lau fringes can be observed far away from the gratings only if the grat-ings are spaced by a half-integer multiple of the Talbot length z_T. The fringe visibility therefore depends on the
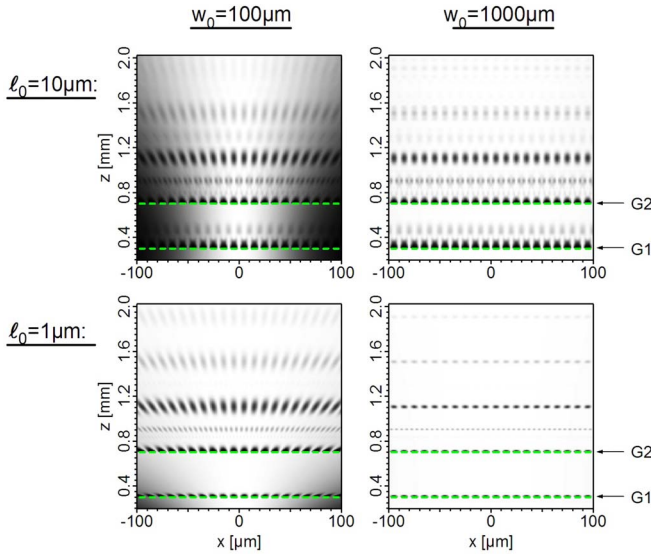
FIG. 4. (Color online) Interference in a Talbot-Lau interferometer. Each row of the intensity in these figures has been normalized to 1. The two gratings have periods of 10 μm, a 42% open fraction, and are located at $z_1 = 0.3$ mm and $z_2 = 0.7$ mm. They are separated by one Talbot length for the wavelength used (500 nm). The figures on the left have an initial beam diameter of $w_0 = 100$ μm and the figures on the right have an initial beam diameter of $w_0 = 1000$ μm. The figures on the top have an initial coherence width of $\ell_0 = 10$ μm, and on the bottom $\ell_0 = 1$ μm. Without the second grating the lower left image would look similar to the bottom center image in Fig. 2. Typically, a third grating G3 would be used as a mask to detect these fringes at $z_3 = 1.1$ mm.

beam's wavelength λ as shown in Fig. 8. The period d' of the Lau fringes is given by

$$d' = \frac{r_x(z_3)}{z_{12}}d \approx \frac{z_{12}+z_{23}}{z_{12}}d, \qquad (20)$$

where the last approximation is valid if the beam has a very small coherence width at G1. Due to the geometric magnification, the fringe period can be much larger than the grating
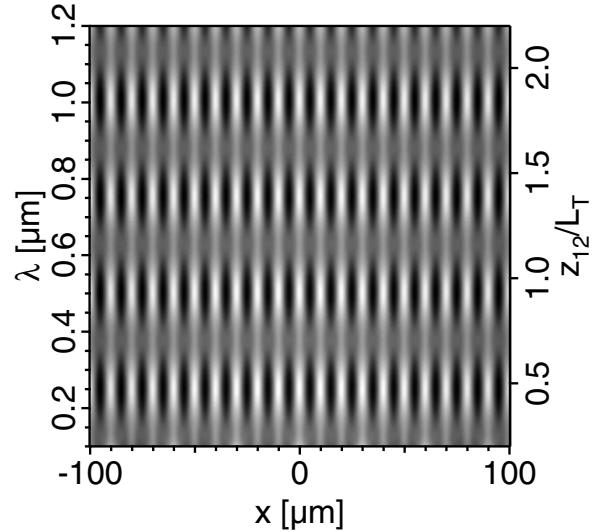

FIG. 5. Fringes in a Talbot-Lau interferometer at the specific location where $z_{23} = z_{12}$, as a function of wavelength λ (left axis) or, alternatively, grating separation z_{12}. The grating separation is expressed in units of the Talbot length, for which $\lambda = 500$ nm is used. A classical ray optics model also predicts fringes at $z_{23} = z_{12}$, but only wave optics correctly predicts how the visibility of the fringes depends on the wavelength.

period and can be imaged directly instead of using a third grating as a mask. The fringe period gets smaller as z_{12} increases. This behavior, along with oscillation of Lau fringe visibility as a function of grating separation, can be seen in Fig. 7. Data showing these effects were obtained with our electron beam Lau interferometer [6].

IV. CONCLUSION

In summary, we derived a general expression, Eq. (18), that can efficiently model the effects of partial coherence and wave-front curvature, in two transverse directions, on interference effects behind one- and two-grating systems. This result is valid in the paraxial (Fresnel) approximation and has
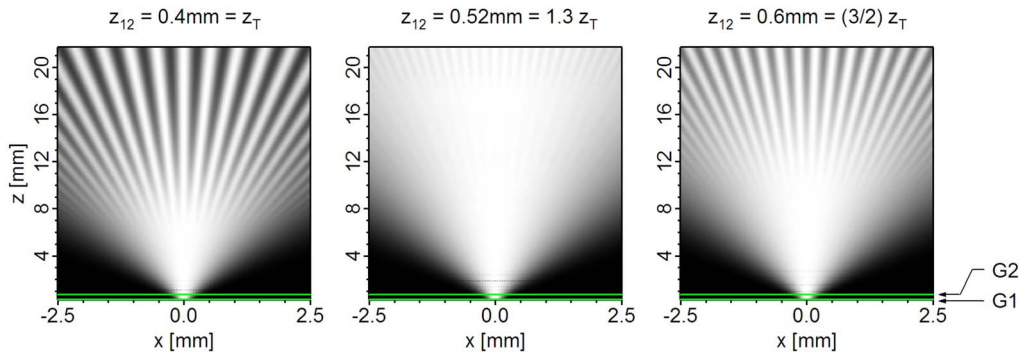

FIG. 6. (Color online) Lau fringes for different grating separations. For presentation purposes, each row (corresponding to position z) of the intensity in these figures has been normalized to 1. In the left image, a $\lambda = 500$ nm incoherent beam $\ell_0 = 1$ μm $= w_0/200 = d/10$ illuminates two gratings spaced by 0.4 mm, which is equal to the Talbot distance ($z_T = 2d^2/\lambda$). In the center image, the gratings are separated by 0.52 mm and the fringes are less visible. In the right image, the gratings are separated by 0.6 mm $= 3z_T/2$, and become visible again. At this larger scale, Talbot-Lau fringes (Fig. 4) are barely visible directly behind the second grating.
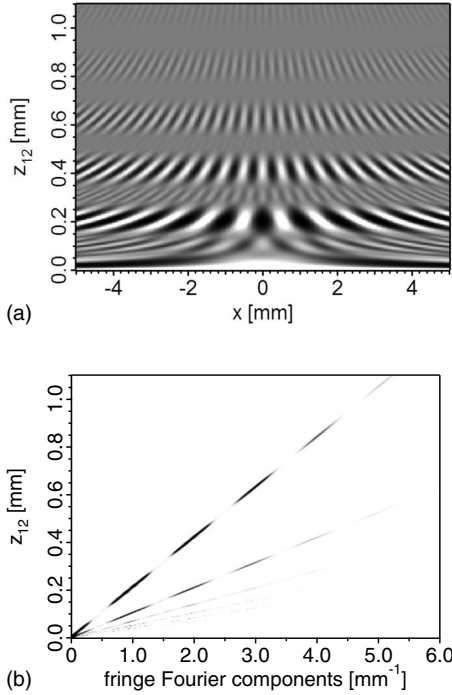
(a)

(b)

FIG. 7. (a) Lau fringe profile, as observed 21 mm from the gratings, versus grating separation z_{12}. Parameters used for this image are 35% open fraction gratings, and an isotropic $\lambda=500$ nm GSM beam with $w_0=200$ μm and $\ell_0=0.1$ μm. (b) Power spectra of Lau fringes versus grating separation z_{12}. Each row in the figure is obtained from the Fourier transform of the fringe intensity profile for a particular grating separation.

been derived for gratings that may have different periods, are arbitrarily located, and can be rotated with respect to each other.

To illustrate the versatility of the model, we simulated the Talbot effect and far-field diffraction behind a single grating, and we simulated Mach-Zehnder, Talbot-Lau, and Lau interferometers. The coherence properties of the specific type of beam we assumed, a GSM beam, evolve in a similar way to other types of beams, so this theory may be useful for mod-
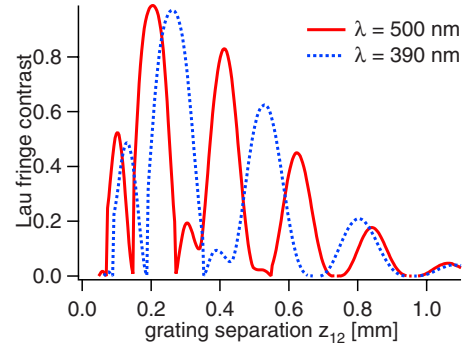

FIG. 8. (Color online) Lau fringe contrast versus grating separation z_{12} with the same parameters used for Fig. 7, for two wavelengths.

eling the role of partial coherence in real matter wave interferometry experiments.

ACKNOWLEDGMENT

APPENDIX

To propagate a general mutual intensity function over a distance z, one can use the paraxial approximation to Zernike's propagation law for partially coherent waves [15,36]:

$$J(\boldsymbol{\rho}_a,\boldsymbol{\rho}_b;z) = \frac{1}{\lambda^2 z^2}\int d\boldsymbol{\rho}_a'\int d\boldsymbol{\rho}_b' e^{-(i\pi/\lambda z)[(\boldsymbol{\rho}_a - \boldsymbol{\rho}_a')^2 - (\boldsymbol{\rho}_b - \boldsymbol{\rho}_b')^2]}$$
$$\times J(\boldsymbol{\rho}_a',\boldsymbol{\rho}_b';0). \tag{A1}$$

A merit of the GSM beam is that its mutual intensity is a simple function of redefined position variables, $\boldsymbol{\rho}\equiv(\boldsymbol{\rho}_a+\boldsymbol{\rho}_b)/2$ and $\Delta\boldsymbol{\rho}\equiv(\boldsymbol{\rho}_b-\boldsymbol{\rho}_a)$, which provides a simpler way to evaluate Eq. (A1):

$$J(\boldsymbol{\rho},\Delta\boldsymbol{\rho};z) = \frac{1}{\lambda^2 z^2}\int d\Delta\boldsymbol{\rho}\int d\boldsymbol{\rho}' e^{-(i2\pi/\lambda z)(\boldsymbol{\rho}'\Delta\boldsymbol{\rho}'-\boldsymbol{\rho}'\Delta\boldsymbol{\rho}-\boldsymbol{\rho}\Delta\boldsymbol{\rho}'+\boldsymbol{\rho}\Delta\boldsymbol{\rho})}$$
$$\times J(\boldsymbol{\rho}',\Delta\boldsymbol{\rho}';0). \tag{A2}$$

[1] L. Liu, Appl. Opt. **28**, 4668 (1989).

[2] S. Chitralekha, K. V. Avudainayagam, and S. V. Pappu, Appl. Opt. **29**, 125 (1990).

[3] J. H. Tu and L. Zhan, Opt. Commun. **82**, 229 (1991).

[4] J. H. Tu and L. Zhan, J. Opt. Soc. Am. A **9**, 983 (1992).

[5] Y. J. Pan and T. Asakura, Opt. Eng. (Bellingham) **32**, 2850 (1993).

[6] A. D. Cronin and B. McMorran, Phys. Rev. A **74**, 061602(R) (2006).

[7] F. F. Medina and G. Pozzi, J. Opt. Soc. Am. A **7**, 1027 (1990).

[8] B. McMorran and A. D. Cronin, e-print arXiv:0804.1162v1.

[9] F. Gori, Opt. Commun. **46**, 149 (1983).

[10] E. Collett and E. Wolf, Opt. Lett. **2**, 27 (1978).

[11] E. Wolf and E. Collett, Opt. Commun. **25**, 293 (1978).

[12] M. Born and E. Wolf, *Principles of Optics*, 7th ed. (Cambridge University Press, Cambridge, U.K., 2005).

[13] L. Mandel and E. Wolf, *Optical Coherence and Quantum Optics* (Cambridge University Press, New York, 1995).

[14] A. Starikov and E. Wolf, J. Opt. Soc. Am. **72**, 923 (1982).

[15] A. T. Friberg and R. J. Sudol, Opt. Commun. **41**, 383 (1982).

[16] B. D. Lu, B. Zhang, and B. W. Cai, J. Mod. Opt. **42**, 289 (1995).

[17] P. De Santis, F. Gori, G. Guattari, and C. Palma, Opt. Commun. **29**, 256 (1979).

[18] B. McMorran, J. Perreault, T. Savas, and A. D. Cronin, Ultramicroscopy **106**, 356 (2006).

[19] Y. Li and E. Wolf, Opt. Lett. **7**, 256 (1982).

[20] K. Patorski, Prog. Opt. **27**, 3 (1989).

[21] C. David, B. Nohammer, H. H. Solak, and E. Ziegler, Appl. Phys. Lett. **81**, 3287 (2002).

[22] D. Malacara-Doblado, Opt. Eng. (Bellingham) **36**, 2016 (1997).

[23] B. Barwick, G. Gronniger, L. Yuan, S. H. Liou, and H. Batelaan, J. Appl. Phys. **100**, 074322 (2006).

[24] D. W. Keith, C. R. Ekstrom, Q. A. Turchette, and D. E. Pritchard, Phys. Rev. Lett. **66**, 2693 (1991).

[25] A. Miffre, M. Jacquey, M. Buchner, G. Trenec, and J. Vigue, Eur. Phys. J. D **33**, 99 (2005).

[26] J. D. Perreault and A. D. Cronin, Phys. Rev. A **73**, 033610 (2006).

[27] V. P. Chebotayev, B. Y. Dubetsky, A. P. Kasantsev, and V. P. Yakovlev, J. Opt. Soc. Am. B **2**, 1791 (1985).

[28] C. Champenois, M. Buchner, and J. Vigue, Eur. Phys. J. D **5**, 363 (1999).

[29] M. S. Chapman, C. R. Ekstrom, T. D. Hammond, J. Schmiedmayer, B. E. Tannian, S. Wehinger, and D. E. Pritchard, Phys. Rev. A **51**, R14 (1995).

[30] J. D. Perreault and A. D. Cronin, Phys. Rev. Lett. **95**, 133201 (2005).

[31] B. Brezger, M. Arndt, and A. Zeilinger, J. Opt. B: Quantum Semiclassical Opt. **5**, S82 (2003).

[32] H. Batelaan, S. Barnet, M. K. Oberthaler, E. Rasel, J. Schmiedmayer, and A. Zeilinger, in *Atom Interferometry*, edited by P. R. Berman (Academic Press, San Diego, 1997), pp. 85–120.

[33] B. Brezger, L. Hackermuller, S. Uttenthaler, J. Petschinka, M. Arndt, and A. Zeilinger, Phys. Rev. Lett. **88**, 100404 (2002).

[34] E. Lau, Ann. Phys. **6**, 417 (1948).

[35] J. Jahns and A. W. Lohmann, Opt. Commun. **28**, 263 (1979).

[36] F. Zernike, Physica (Amsterdam) **5**, 785 (1938).